Development of an adaptive rolling tuned mass damper for structural vibration control under random directional excitation

(Article begins on next page)

Development of an adaptive rolling tuned mass damper for structural vibration control

Yifan Luo[a, b], Hongxin Sun [a, b]*, Wei Wang[b], Jintao Li[b], Ta Chih Hung [c], Wenxi Wang[d], Stefano Lenci[e]

a Sanya Institute of Hunan University of Science and Technology, Sanya 572024, Hainan, China

b Hunan Provincial Key Laboratory of Structural Engineering for Wind Resistant and Vibration Control, and School of Civil Engineering, Hunan University of Science and Technology, Xiangtan 411201, Hunan, China

c Naval Architecture and Marine Engineering, University of Michigan, Ann Arbor, MI 48109, USA

d National Key Laboratory of Bridge Safety and Resilience, Key Laboratory for Bridge and Wind Engineering of Hunan Province, Shock and Vibration Technology Research Center, Hunan University, Changsha 410082, Hunan, China

e Department of Civil and Building Engineering and Architecture, Polytechnic University of Marche, Ancona 60131, Italy.

Email addresses: ceyfluo@hnust.edu.cn (Yifan Luo, first author), cehxsun@hnust.edu.cn (Hongxin Sun, corresponding author*)

Abstract: In the natural environment, the external loads suffered by slender structures, such as wind loads, are usually random in their direction. To reduce the random directional vibration of structures, a novel Adaptive Rolling Tuned Mass Famper (ARTMD) is proposed, which consists of a spherical oscillator, a track, a rotating bearing, and a hemispherical cavity. When the main structure vibrates, the internal trajectory of the ARTMD can be adjusted adaptively to the displacement direction of the main structure by the rotating bearing under the action of the moment of inertia of the spherical oscillator. To demonstrate ARTMD's adaptive vibration damping performance, the dynamic model of a single degree of freedom (SDOF) structure coupled with an ARTMD is derived based on the energy method. The optimal design of the ARTMD is conducted based on the H_∞ optimization criterion, whose object is to minimize the structural displacement in the frequency domain. Subsequently, the performance of ARTMD on the SDOF structure in vibration control and adaptive adjustment is examined by numerical simulations and the experiments, respectively. Result shows that the control performances of the ARTMD are better than those of the traditional unidirectional Tuned Rolling Mass Damper (TRMD) where the direction of the external excitation is inconsistent with the direction of the damper track, thanks to the automatic adjustment of the track to the excitation direction.

Key words: Vibration control; Adaptive vibration control; Tuned rolling mass damper.

1. Introduction

Slender structures, such as wind turbines and chimneys, are highly susceptible to wind effects. Given that severe wind-induced vibrations can compromise both safety and comfort, controlling such vibrations becomes essential in the design of these structures. In recent years, structural vibration control strategies have emerged as an effective solution and have been increasingly applied to mitigate vibrations in slender structures. These strategies are generally categorized into three types: passive, active, and semi-active control [1-2]. Among them, passive control systems are the most widely adopted, primarily due to their ability to operate without external energy input.

Tuned Rolling Mass Damper (TRMD) is a passive vibration control device that operates through the reciprocating rolling motion of a mass (typically a sphere or cylinder) on a concave surface [3]. The reaction force generated by this motion counteracts vibrations in the primary structure. Compared to traditional Pendulum Tuned Mass Dampers (PTMD), the TRMD offers a significantly more compact vertical design, making it a subject of extensive research [4-6].

Current applications of TRMDs primarily focus on suppressing wind-induced vibrations in tall, slender structures (such as TV towers [7, 8] and offshore wind turbines [9-13]) and reducing the seismic response of multi-story buildings [14, 15]. To enhance performance, researchers have investigated hybrid systems that combine TRMDs with pounding Tuned Mass Dampers (TMDs) [16, 17] or adding additional damping to the TRMD by oil-filing the hollow ball [18]. Beyond civil engineering, TRMDs have been extended to mechanical engineering and medical equipment for controlling device vibrations [19] and even assisting in the treatment of patients with hand tremors [20]. These diverse studies collectively demonstrate the outstanding advantages of TRMDs in space-saving design and vibration control performance.

However, most existing studies on TRMDs are based on structural vibration control in two-dimensional planes. Consequently, the potential of TRMDs for bidirectional vibration reduction remains underexplored. This research gap is particularly notable given the growing interest in multi-directional vibration control [21-32]. Náprstek et al. [33-36] developed a three-dimensional model accounting for the six degrees of freedom of a sphere moving inside a spherical concave container to investigate the nonlinear behavior of TRMDs. The study found that TRMDs maintain effective vibration control capabilities even under broadband random excitation—commonly used in such studies—and in conditions with very limited vertical space. However, the research also revealed that due to the highly nonlinear nature of the system, the sphere exhibits multiple extreme motion trajectories within the spherical concave track, which adversely impacts the TRMD's vibration reduction efficiency.

Based on the aforementioned issues, this paper proposes an Adaptive Rolling Tuned Mass Damper (ARTMD) aimed at addressing the need for vibration control in random directions of structures. The study begins with an investigation into the dynamic characteristics of the ARTMD, establishing a dynamic model of the coupled ARTMD and single-degree-of-freedom (SDOF) structural system using the energy method (Sect. 2). Subsequently, based on H_∞ algorithm with the optimization objective of minimizing the peak displacement of the primary structure in the frequency domain, an optimization analysis of the ARTMD's vibration control design parameters is conducted (Sect. 3). Finally, vibration control experiments on a single-story frame structure with the ARTMD are carried out to further validate its adaptive vibration control performance, with comparisons made against the traditional unidirectional TRMD (Sect. 4). The paper ends with some conclusions (Sect. 5).

2. Coupled model of the ARTMD on the SDOF structure

2.1 The working principle of ARTMD

For a slender structure, only a SDOF reduced order model can be considered since a MDOF structure can be simplified into an SDOF primary structure based on the mode decomposition methods, in particular in the optimal design process [37-40]. The theoretical model of a linear SDOF primary structure with a ARTMD is shown in Fig. 3, where m_s, k_s and c_s, represent the mass, stiffness, and damping of the primary structure, respectively. The ARTMD consists of an oscillator (a ball), a semi-circular track, a rotating bearing, two plain bearings and a hemispherical container. The track contains two splints that restrict the ball from sliding within the track.

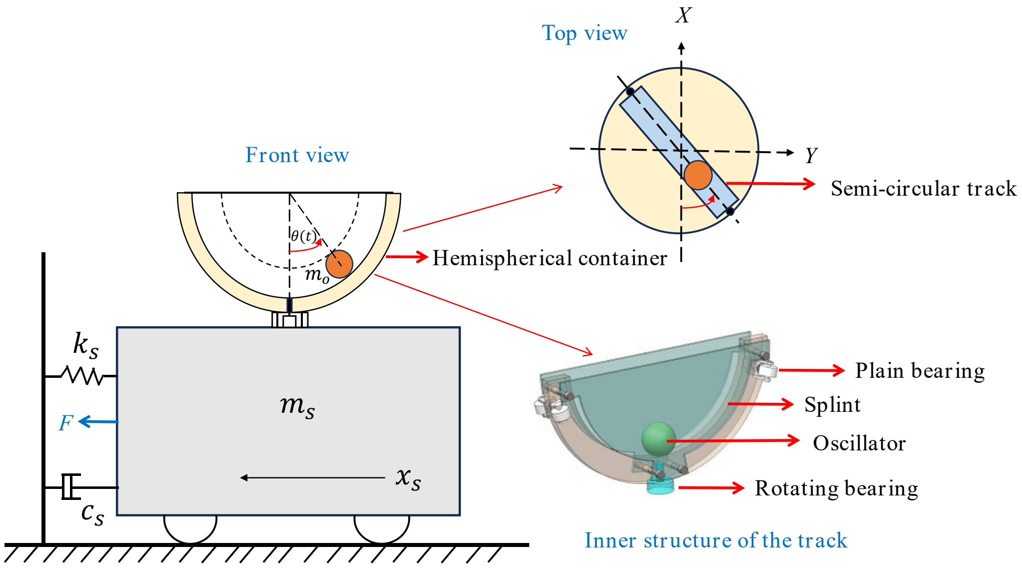

Fig. 3 Coupled system of a SDOF structure with a ARTMD

When ARTMD is operating, the oscillator's force diagram in the track plane and in the vertical track plane is shown in Fig. 4. x_s is defined as the displacement of the controlled structure relative to the ground (see Fig. 3). R, r, r_1 represent the track's radius, the oscillator's radius, and the track's thickness, respectively. θ is the angular displacement of the oscillator relative to the center line of the track. φ represents the angle between the direction of the track and the displacement direction of the main structure. The mass of the oscillator, two splints, track and hemispherical container are m_o, m_1, m_2 and m_3, respectively. When subjected to horizontal excitation, the main structure shifts horizontally while the oscillator rolls along the track. If the track's axial direction is not aligned with the direction of excitation, the component of the oscillator's inertial force acting on the vertical track's surface creates a rotational torque. This torque causes the track to rotate around the bolt bearing, allowing it to adaptively adjust its direction until it aligns with the excitation direction. Structural energy is dissipated by the friction between the ball and the track, as well as the friction between the track and the bolt bearing.

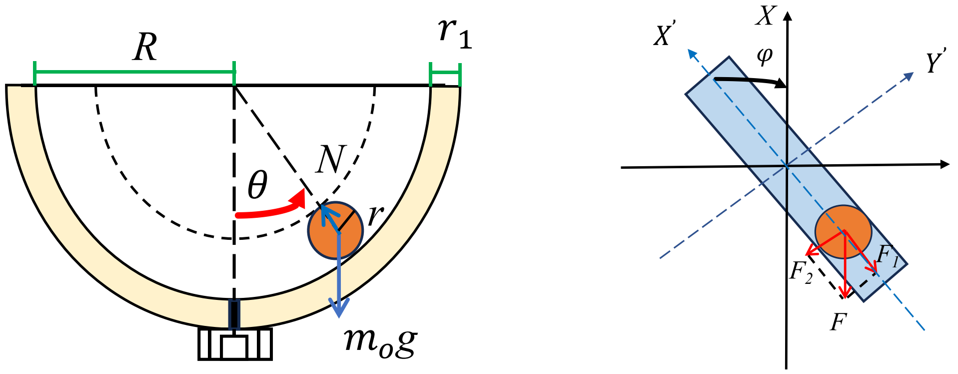

Fig. 4 Schematic diagram in the track plane and in the vertical track plane

2.2 Dynamic model of the coupled system with the ARTMD

2.2.1 Modeling approach

The coupled system of the SDOF structure with an attached ARTMD is established based on the Lagrange method, whose specific equations are expressed as follows,

$$\frac{\mathrm{d}}{\mathrm{d}t}\left(\frac{\partial T}{\partial \dot{q}_i}\right)-\frac{\partial T}{\partial q_i}+\frac{\partial V}{\partial q_i}=Q_i^{nc}\,, i=1,2,3, \tag{1}$$

where T and V represent the system's kinetic energy and potential energy (including gravitational and elastic potential energies), respectively. q_i is the generalized coordinate.

2.2.2 Kinetic energy

According to the transformation of the coordinate system, the generalized coordinates of the oscillator are obtained, and then the kinetic energy of the oscillator is derived. The geodetic coordinate system $OXYZ$ represents the fixed coordinate system, whereas the orbit plane $O'X'Y'Z'$ represents the movable coordinate system. The coordinate system diagram is shown in Fig. 5.

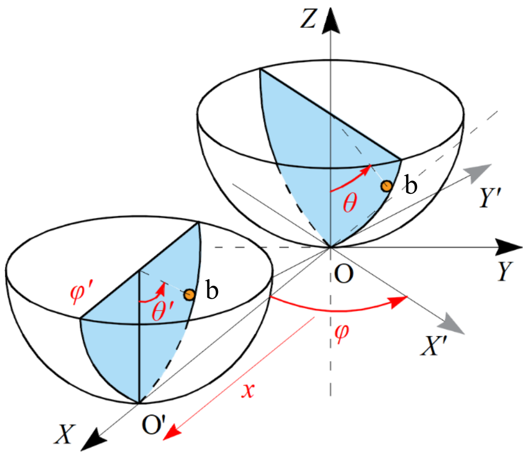

Fig. 5 Diagram of the ARTMD in coordinate system

In the $O'X'Y'Z$ coordinate system, the X and Z coordinates of the oscillator center b meet the following conditions because of the motion trajectory,

$$\begin{cases} x_b' = \rho\sin\theta, \\ z_b' = \rho(1-\cos\theta), \\ (x_b')^2 + (z_b' - \rho)^2 = \rho^2 t. \end{cases} \tag{2}$$

From the relative coordinate system $OX'Y'Z$ to the fixed coordinate system $OXYZ$, there is a rotation about the Z axis with the rotation matrix $\mathbf{T}$ as follows, and a translation x along the X direction:

$$\mathbf{T} = \begin{bmatrix} \cos\varphi & -\sin\varphi & 0 \\ \sin\varphi & \cos\varphi & 0 \\ 0 & 0 & 1 \end{bmatrix}. \tag{3}$$

Therefore, the coordinates of the oscillator center b in $OXYZ$ can be expressed as:

$$\begin{bmatrix} x_b \\ y_b \\ z_b \end{bmatrix} = \begin{bmatrix} \cos\varphi & -\sin\varphi & 0 \\ \sin\varphi & \cos\varphi & 0 \\ 0 & 0 & 1 \end{bmatrix} \begin{bmatrix} x_b' \\ y_b' \\ z_b' \end{bmatrix} + \begin{bmatrix} x \\ 0 \\ 0 \end{bmatrix}. \tag{4}$$

Eq. (4) can be simplified as follows:

$$\begin{cases} \dot{x}_b = x + \rho\sin\theta\cos\varphi, \\ \dot{y}_b = \rho\sin\theta\sin\varphi, \\ \dot{z}_b = \rho(1-\cos\theta). \end{cases} \tag{5}$$

The velocities are then

$$\begin{cases} \dot{x}_b = \dot{x} + \dot{\theta}\rho\cos\theta\cos\varphi - \dot{\varphi}\rho\sin\theta\sin\varphi, \\ \dot{y}_b = \dot{\theta}\rho\cos\theta\sin\varphi + \dot{\varphi}\rho\sin\theta\cos\varphi, \\ \dot{z}_b = \dot{\theta}\rho\sin\theta. \end{cases} \tag{6}$$

The square of absolute velocity of the oscillator is then

$$v_b^2 = \dot{x}_b^2 + \dot{y}_b^2 + \dot{z}_b^2 = \dot{x}^2 + \dot{\varphi}^2\rho^2\sin^2\theta + \dot{\theta}^2\rho^2 + 2\dot{x}\dot{\theta}\rho\cos\theta\cos\varphi - 2\dot{x}\dot{\varphi}\rho\sin\theta\sin\varphi. \tag{7}$$

The kinetic energy of the system consists of the kinetic energy of the main structure, the rotational kinetic energy of the track system around the Z axis, the translational and the rotational kinetic energy of the oscillator, and the rotational kinetic energy of the oscillator around the Z axis. The specific calculation formula is as follows:

$$T^c = \frac{1}{2}(m_s + m_1 + m_2 + m_3)\dot{x}^2 + \frac{1}{2}m_0 v_b^2 + \frac{1}{2}J_1\omega^2 + \frac{1}{2}(J_2 + J_3)\dot{\varphi}^2, \tag{8}$$

where, $\rho = R - r$ is the radius difference between the arc path and the oscillator. ω is the oscillator's angular velocity as it rotates about its own center, $\omega = \rho\dot{\theta}/r$. J_1 is the rotational inertia of the oscillator's rotation about its own center. J_2 is the rotational inertia of the two splints and the track around Z axis. J_3 is the rotational inertia of the oscillator around Z axis. They are given by

$$\begin{cases} J_1 = \frac{2}{5} m_0 r^2, \\ J_2 = 2\left(\frac{1}{4} m_1 R^2 + m_1 r^2\right) + \frac{1}{2} m_2 r_1^2, \\ J_3 = m_0 \rho^2 \sin^2\theta. \end{cases} \tag{9}$$

Substituting Eqs. (7) and (9) into Eq. (8), the kinetic energy can be expressed as

$$T^c = \frac{1}{2}(m_s + m_1 + m_2 + m_3)\dot{x}^2 + \frac{1}{2} m_0(\dot{x}^2 + \dot{\varphi}^2\rho^2\sin^2\theta + \dot{\theta}^2\rho^2 + 2\dot{x}\dot{\theta}\rho\cos\theta\cos\varphi$$

$$-2\dot{x}\dot{\varphi}\rho\sin\theta\sin\varphi) + \frac{1}{5} m_0\rho^2\dot{\theta}^2 + \dot{\varphi}^2\left(\frac{1}{5} m_0 r^2 + \frac{1}{2} m_0\rho^2\sin^2\theta + \frac{1}{4} m_1 R^2 + m_1 r^2 + \frac{1}{4} m_2 r_1^2\right). \tag{10}$$

2.2.2 Potential energy

The potential energy of the coupled system includes the elastic potential energy of the main structure, the gravitational potential energy of the oscillator and the elastic potential energy of the orbit. Therefore, the potential energy of the system can be written as

$$V^c = m_0 g\rho(1 - \cos\theta) + \frac{1}{2} k\varphi^2 + \frac{1}{2} k_s x^2, \tag{11}$$

where k is defined as the reset stiffness of the splint, which is mainly provided by the resultant force of the collision force between the splint and the oscillator, and the friction force between the track and the rotating bearing.

2.2.3 Virtual work done by the non-conservative forces

The virtual work of the system mainly includes work done by external excitation, work done by structure's inherent damping force, work done by rolling friction torque of the ball in the track and work done by bearing friction. To simplify the calculation, the contact friction between the rail system and the hemispherical container is ignored. The specific calculation formula is expressed as

$$\delta W = F - C\dot{x}\delta x - \frac{\dot{\theta}}{|\dot{\theta}|} f_1 \delta(\psi + \theta) - \frac{\dot{\varphi}}{|\dot{\varphi}|} f_2 \delta\varphi, \tag{12}$$

where F is the external force operating on the main structure (see Fig. 3). ψ represents the angle that the oscillator's centre deviates from its equilibrium location. δx, $\delta\theta$, $\delta\varphi$ represent the primary structure's virtual displacement in the horizontal direction, the rolling oscillator's virtual rotational displacement, and the track system's virtual rotational displacement, respectively. f_1 is the non-conservative rolling friction torque and f_2 is the bearing friction torque, which are calculated as follows:

$$\begin{cases} f_1 = \mu_1 m_0\left(g\cos\theta + \rho\dot{\theta}^2\right), \\ f_2 = \frac{1}{2}\mu_2 d(m_0 + m_1 + m_2), \end{cases} \tag{13}$$

where μ_1, μ_2 and d represent the rolling friction coefficients, the rotating bearing friction coefficients and the rotating bearing radius, respectively.

For the convenience of modeling, we assume that the rolling oscillator only rolls purely along the track and does not slide. The following relationship can be obtained:

$$\delta(\varphi + \theta)r = R\delta\theta. \tag{14}$$

Combined with Eq. (14) and Eq. (13), Eq. (12) can be written as

$$\delta W = F - c_s\dot{x}\delta x - \frac{\dot{\theta}}{|\dot{\theta}|}\mu_1 m_0\left(g\cos\theta + \rho\dot{\theta}^2\right)\frac{R}{r}\delta\theta - \frac{1}{2}\frac{\dot{\varphi}}{|\dot{\varphi}|}\mu_2 d(m_0 + m_1 + m_2)\delta\varphi. \tag{15}$$

According to the virtual work calculated in Eq. (15), the nonconservative forces are

$$\begin{cases} Q_1^{nc}(x) = (F - c_s\dot{x}), \\ Q_2^{nc}(\theta) = -\frac{\dot{\theta}}{|\dot{\theta}|}\mu_1 m_0\left(g\cos\theta + \rho\dot{\theta}^2\right)\frac{R}{r}, \\ Q_2^{nc}(\varphi) = -\frac{1}{2}\frac{\dot{\varphi}}{|\dot{\varphi}|}\mu_2 d(m_0 + m_1 + m_2). \end{cases} \tag{16}$$

Assuming that the oscillator's and orbit's angular displacement is small, and substituting Eqs. (10), (11) and (16) into Eq. (1), the system's motion equation can be expressed as

$$(m_s + m_1 + m_2 + m_3 + m_0)\ddot{x} + m_0\ddot{\theta}\rho + c_s\dot{x} + k_s x = F, \tag{17}$$

$$\frac{7}{5}m_o\rho^2\ddot{\theta} + m_o\rho\ddot{x} + m_o g\rho\theta = -\frac{\dot{\theta}}{|\dot{\theta}|}\mu_1 m_o g\frac{R}{r}, \tag{18}$$

$$\left(\frac{2}{5}m_o r^2 + \frac{1}{2}m_1 R^2 + 2m_1 r^2 + \frac{1}{2}m_2 r_1^2\right)\ddot{\varphi} + k\varphi = -\frac{1}{2}\frac{\dot{\varphi}}{|\dot{\varphi}|}\mu_2 d(m_o + m_1 + m_2). \tag{19}$$

The equations of motion of the ARTMD system can be written in the matrix equations as

$$\mathbf{M}\ddot{\mathbf{q}} + \mathbf{C}\dot{\mathbf{q}} + \mathbf{K}\mathbf{q} = \mathbf{F}, \tag{20}$$

where

$$\mathbf{X} = [x \quad \theta \quad \varphi]^T,$$

$$\mathbf{F} = \left[F \quad -\frac{\dot{\theta}}{|\dot{\theta}|}\mu_1 m_o g\frac{R}{r} \quad -\frac{1}{2}\frac{\dot{\varphi}}{|\dot{\varphi}|}\mu_2 d(m_o + m_1 + m_2)\right]^T,$$

$$\mathbf{M} = \begin{bmatrix} m_s + m_1 + m_2 + m_3 + m_0 & m_o\rho & 0 \\ m_o\rho & \frac{7}{5}m_o\rho^2 & 0 \\ 0 & 0 & \frac{2}{5}m_o r^2 + m_1(\frac{1}{2}R^2 + 2r^2) + \frac{1}{2}m_2 r_1^2 \end{bmatrix},$$

$$\mathbf{C} = \begin{bmatrix} c_s & 0 & 0 \\ 0 & 0 & 0 \\ 0 & 0 & 0 \end{bmatrix},$$

$$\mathbf{K} = \begin{bmatrix} k_s & 0 & 0 \\ 0 & m_o g\rho & 0 \\ 0 & 0 & k \end{bmatrix}.$$

3 Parametric analysis of the ARTMD

3.1 Parametric Optimization of the tuning parameters

Since the influence of friction is considered in the process of modeling, the dynamic model of ARTMD includes the influence of nonlinear factors. Therefore, we employ numerical methods to determine the coupled system's response and to perform optimal design of the ARTMD parameters. Specifically, the Newmark method is used to solve the coupled system's response, and the H_∞ optimization criterion is adopted for parameter optimization, whose target is to minimize the peak value of the structural vibration in frequency domain.

To facilitate the analysis of structural response and the parameter optimization of ARTMD in the frequency domain, the dimensionless parameters introduced in Tab. 1 are used.

Tab. 1 Dimensionless parameters in the coupled system

Symbols	Definitions
ω	External frequency
$\omega_s = \sqrt{k_s/m_s}$	Natural frequency of the main structure
$\omega_a = \sqrt{5g/7\rho}$	Natural frequency of the ARTMD
$\zeta_s = 2m_s\omega_s$	Damping ratio of the main structure
$\alpha = m_o/m_s$	Mass ratio of the ARTMD to the main structure
$\lambda = \omega_a/\omega_s$	Frequency ratio of the ARTMD
$\beta = \omega/\omega_s$	External frequency ratio

The target of the H_∞ optimization criterion is to minimize the peak value of the structural vibration x, and the objective function J is

$$J = \min_{\lambda}\left[\max_{\beta}(\mathrm{DMF}_s(\beta))\right], \tag{21}$$

where $\mathrm{DMF}_s(\beta)$ denotes the dynamic amplification coefficient of the structural displacement whose expression is as follows:

$$\mathrm{DMF}_s(\beta) = \frac{X(\beta)k_s}{f_0}. \tag{22}$$

$X(\beta)$ is the steady-state response amplitude of the controlled structure under harmonic excitation $F_h(t) = f_0 \sin(\beta\omega_s t)$. Since the control kinetic equation of the ARTMD contains nonlinear factors, $\mathrm{DMF}_s(\beta)$ cannot be expressed by easy formulas. Therefore, this study applies the genetic algorithm to search for the optimal design frequency ratio λ_{opt}.

When optimizing, the model parameters of subsequent experiments are selected in the numerical simulation. The main structural parameters of the coupled system are shown in Tab. 2.

Tab. 2 Structural parameters of the coupled system

	Parameters name	Symbols	Value
Main Structure	Mass		15.36 kg
	Stiffness	k_s	1161.64 N/m
	Damping		2.11 N • s/m
ARTMD	Rolling friction coefficient of the track	μ_1	0.0018
	Friction coefficient of the rotating bearing	μ_2	0.002
	Splint mass		0.0035 kg
	Track mass		0.28 kg
	Hemispherical container mass	m_3	0.5 kg
	Track thickness	r_1	0.002 m
	Rotational stiffness	k	1e-04 N·m/rad

In the optimization process, the initial angle φ_0 between the direction of the track and the displacement direction of the main structure is assumed $\pi/6$. Tab. 3 lists the final optimization results of the searched frequency ratio λ_{opt} and the corresponding DMF for different mass ratios. Tab. 3 demonstrates that as the mass ratio increases, the optimal frequency ratio λ_{opt} gradually decreases, and the DMF_s also gradually decreases, but the rate of peak reduction gradually slows down. To further verify the accuracy of the optimization results, Fig. 6 draws the frequency response curve of the structural displacement DMF under various mass ratios. It is confirmed that the DMF decreases progressively as the mass ratio increases, indicating that the vibration damping effect increases as the mass ratio increases. Additionally, the three peaks of the frequency amplitude response curve corresponding to each α are approximately equal, indicating that the parameter optimization has produced satisfactory results.

Tab. 3 Optimal frequency ratios of the ARTMD and corresponding maximum DMF under different mass ratios

Mass ratio α	Optimal frequency ratio λ_{opt}	Maximum DMF_s
1%	0.9838	14.1361
2%	0.9656	11.6424
3%	0.9648	10.5341
4%	0.9624	9.8431
5%	0.9390	9.3149

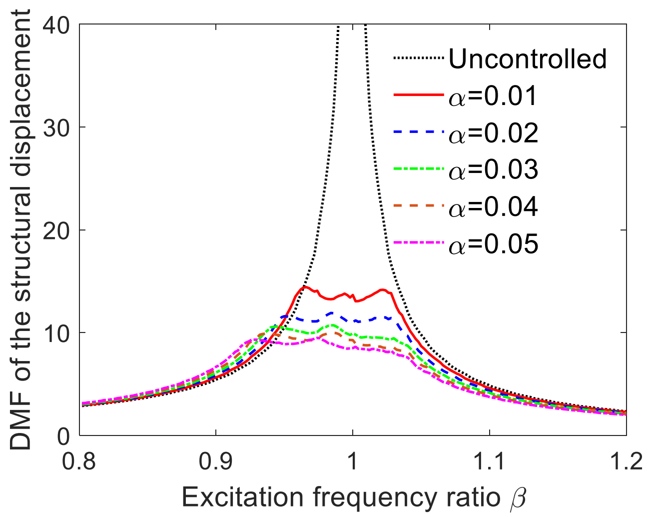

Fig. 6 Dynamic magnification factor curves of the structural displacement under the ARTMD control with different mass ratios

To further analyze the performance advantages of ARTMD, the TRMD under the same conditions is introduced for comparison. The initial angle φ_0 includes four working conditions, which are set to 0 degrees, 30 degrees, 45 degrees and 60 degrees respectively. The biggest difference between TRMD and ARTMD is whether the track can rotate adaptively. Taking the mass ratio of 0.02 as a case study, as shown in Fig. 7, it can be observed that when the initial angle φ_0 is zero, the vibration reduction performance of ARTMD is completely consistent with that of TRMD, as expected. However, when the initial angle φ_0 is not 0, due to the advantage of adaptive vibration reduction, the peak vibration reduction effect of ARTMD in the oscillation region is better than that of TRMD, and the vibration side effects in the non-oscillation region are also less than that of TRMD. In addition, with the gradual increase of the initial angle φ_0, the vibration reduction advantage of ARTMD is gradually improved compared with TRMD. Specifically, when φ_0 is 30, 45 and 60 degrees, respectively, the peak value of DMF_s of the ARTMD is 13.4 %, 31.3% and 50.0% lower than that of TRMD.

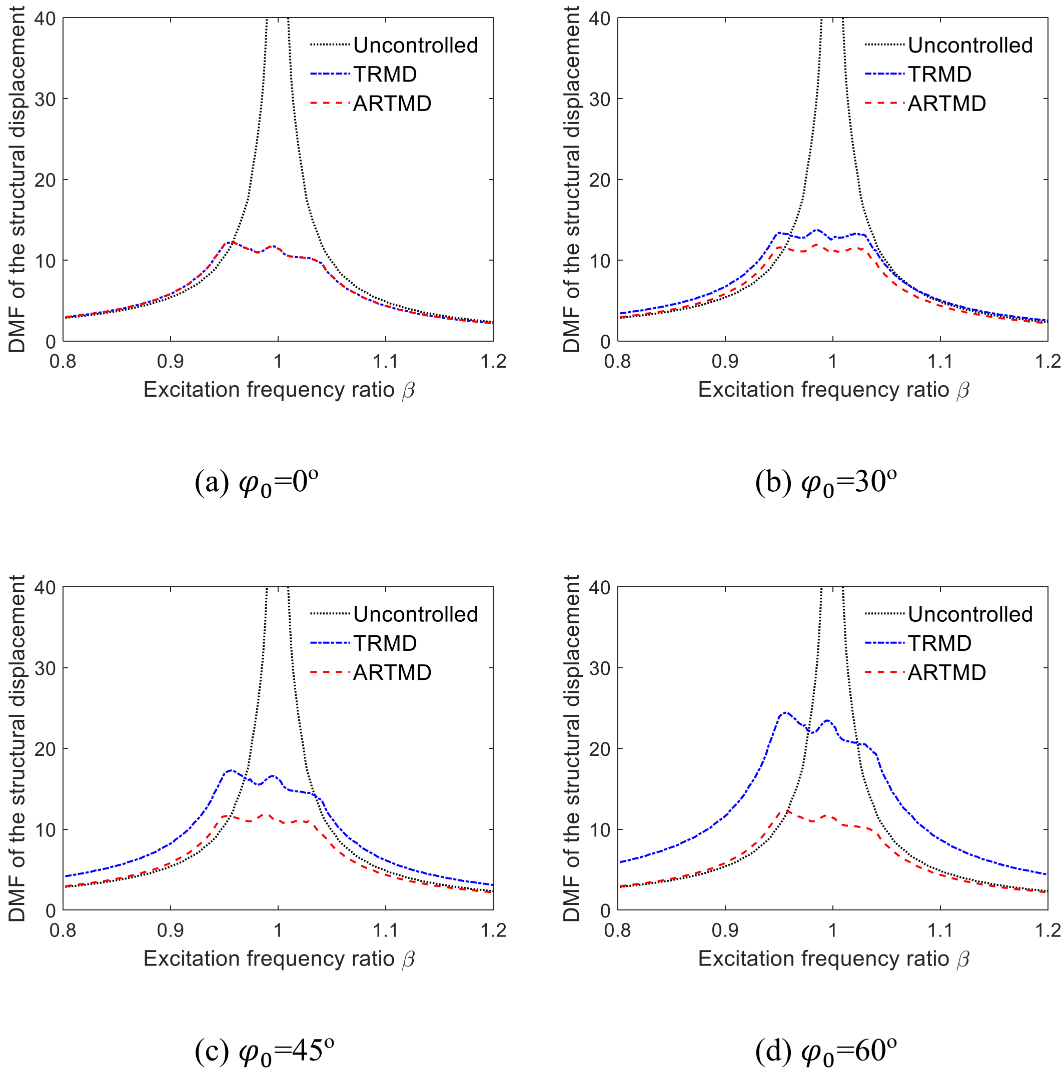

(a) φ_0=0°　　(b) φ_0=30°

(c) φ_0=45°　　(d) φ_0=60°

Fig. 7 Dynamic magnification factor curves of the structural displacement for different systems with different initial φ_0 (α=0.02)

3.2 Analysis of the influence of related design parameters

To further optimize the design of ARTMD we analyze the influence of other system design parameters on the ARTMD vibration reduction performance, including the rolling friction coefficient μ_1 of the track, the friction coefficient μ_2 of the rotating bearing, the splint mass m_1, the track mass m_2 and the rotational stiffness *k*. Fig. 8 shows the influence of five parameters on the dynamic magnification factor curves of the structural displacement. It can be noted that the friction coefficient μ_1 has a major effect, while the others have a negligible influence on the response. Specifically, with the increase of friction coefficient μ_1, the peak value of the DMF curve decreases first and then increases. When μ_1 is 0.0018, the performance of the ARTMD is optimal.

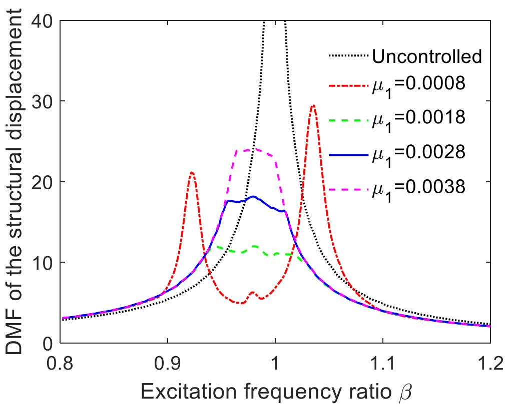

(a)

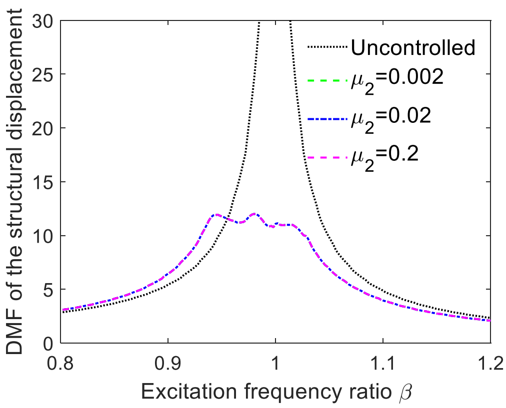

(b)

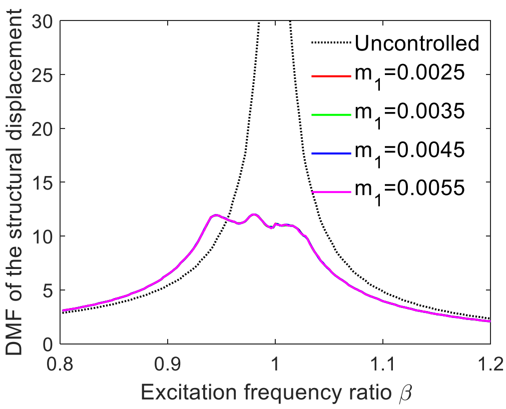

(c)

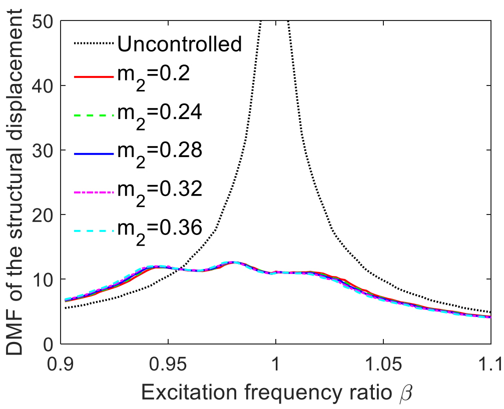

(d)

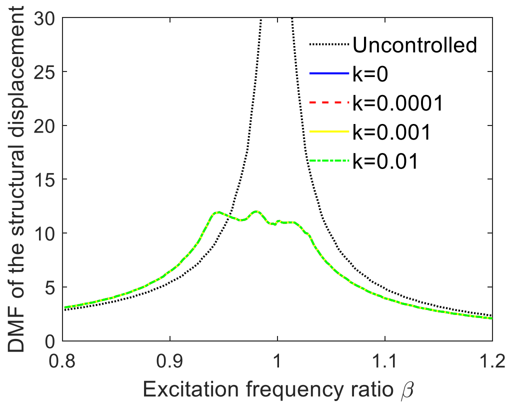

(e)

Fig. 8 The influence of different structural parameters on the dynamic magnification factor curves of the structural displacement: (a) friction coefficient μ_1; (b) friction coefficient μ_2; (c) splint mass m_1; (d) track mass m_2; (e) rotational stiffness k

4 Experimental validation of ARTMD's adaptive control performance

4.1 Design of test model

To verify the actual vibration reduction effect and adaptive function of ARTMD, a single-layer platform frame model is selected as the controlled structure of the test, as shown in Fig. 9(a). The controlled structure model is composed of four aluminum alloy plates as columns, fixed on the top of the large stiffness stainless steel platform plate, and ARTMD is installed on the plate. For ARTMD, nylon with low density is selected as the hemispherical cavity material. The arc track is made of aluminum alloy. The side plate is acrylic plate, which is fixed on both sides of the track. The rolling ball vibrator is made of stainless steel. The specific test model is shown in Fig. 9(b). The processing parameters of the test model correspond to the previous simulation design and parameter optimization results, and the mass ratio of ARTMD is selected as 2%. The specific experimental model parameters are shown in Table 4. A laser displacement sensor and a high-speed camera are used to collect the displacement response of the structure and the rotation angle of the track, respectively.

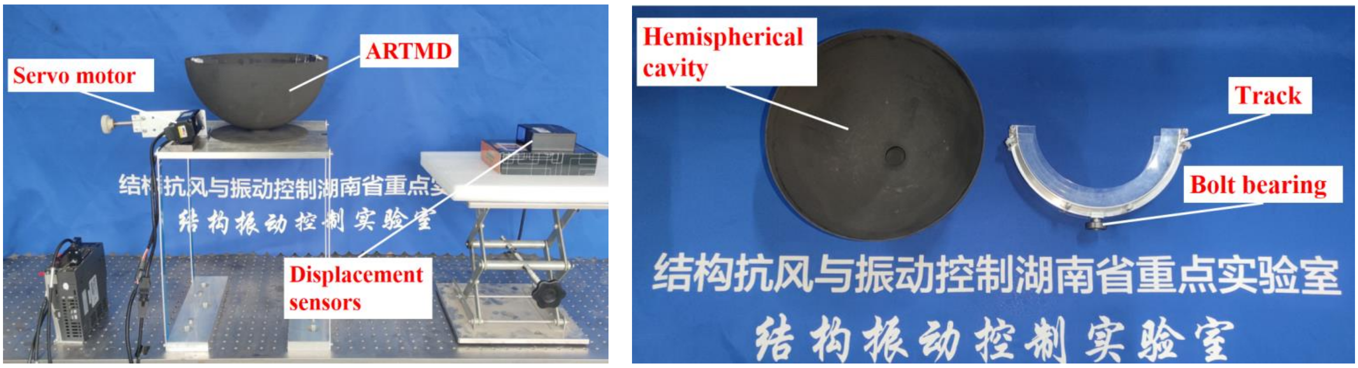

(a) (b)

Fig. 9 Photograph of (a) the main structure and (b) the ARTMD in the experiment

Tab. 4 The parameters of main structure and ARTMD

	Parameters name	Symbols	Value
Main Structure	Mass		15.36 kg
	Stiffness	k_s	1161.64 N/m
	Damping		2.11 N • s/m
ARTMD	Oscillator mass		0.307 kg
	Splint mass		0.0035 kg
	Track mass		0.28 kg
	hemispherical container		0.5 kg
	Oscillator radius	r	0.021 m
	Track radius	R	0.125 m
	Rotating bearing radius	d	0.015 m
	Track thickness	r_1	0.002 m
	Rolling friction coefficient of the track	μ_1	0.0018
	Friction coefficient of the rotating bearing	μ_2	0.002
	Rotational stiffness		1e-04 N·m/rad

4.3 Experimental results

4.3.1 Free vibration

To verify the accuracy of the dynamic model and parameter optimization established by ARTMD, the experimental and theoretical results comparison under free vibration is firstly carried out. The experimental and simulated time histories of the structural displacement curve under the control of ARTMD with different initial angle φ_0 are shown in Fig. 10. It can be observed that the experimental model curve is basically consistent with the theoretical one, which proves the accuracy of the theoretical model of Section 2.

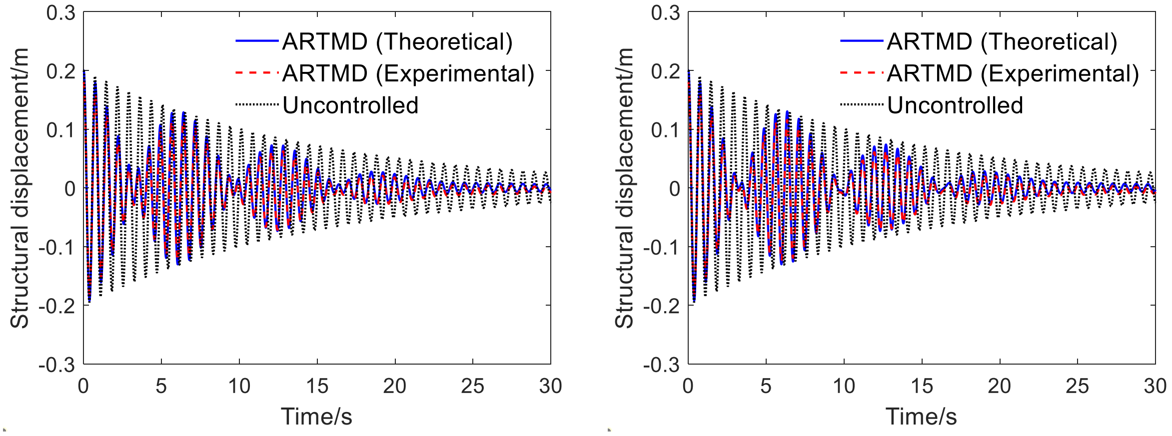

(a) φ_0=30°

(b) φ_0=60°

Fig. 10 Time histories of the structural displacement with different initial angle φ_0 under free vibration

4.3.2 Harmonic excitation

In this section, we carried out a comparative experiment on the vibration reduction performance of ARTMD and TRMD under harmonic excitation. The amplitude of the harmonic excitation is f_0=2N, while its circular frequency is $\beta=2\pi f_1$=14.26rad/s, with an excitation frequency ratio of 1.005. The initial conditions for ARTMD are all set to 0 except for the initial φ_0. The time history curves of the structural displacement and corresponding root mean square (RMS) performance evaluation indexes with different φ_0 are shown in Fig. 11 and Table. 5.

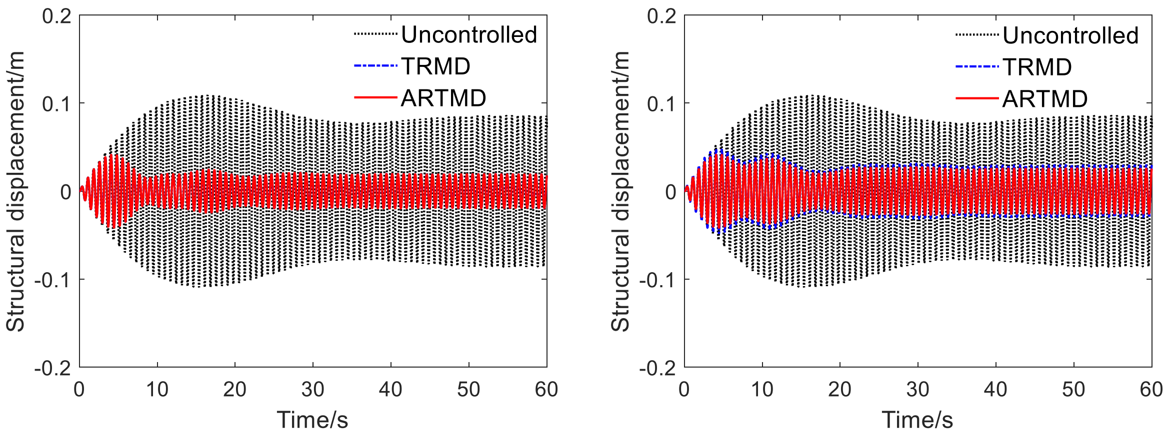

(a) φ_0=0°

(b) φ_0=30°

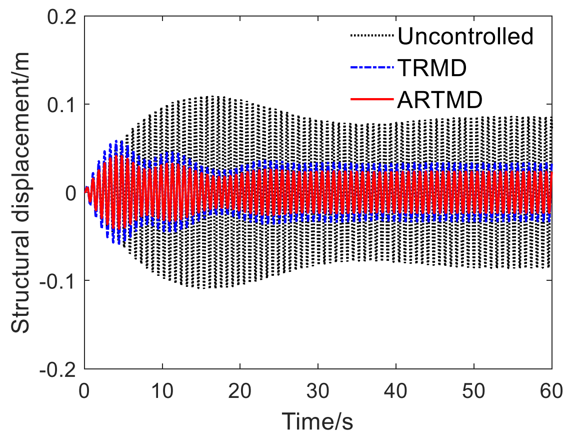

(c) φ_0=45°

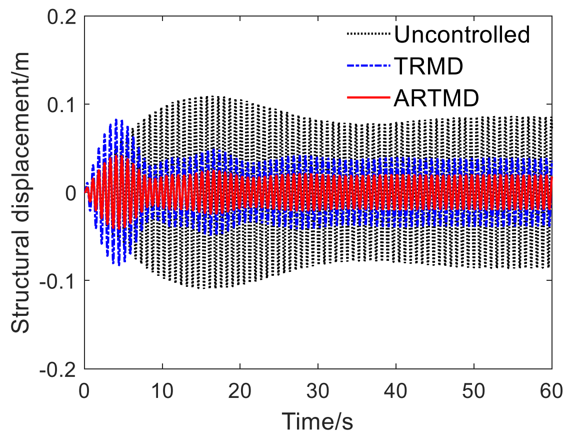

(d) φ_0=60°

Fig. 11 Time histories of the structural displacement with different initial angle φ_0 under harmonic excitation

Tab. 5 The RMS value of the steady-state structural displacement and related vibration reduction rate of different systems under harmonic excitation with different initial angle φ_0

	φ_0	0°	30°	45°	60°
Uncontrolled structure	RMS displacement (mm)	60.8	60.8	60.8	60.8
TRMD	RMS displacement (mm)	13.6	20.9	23.5	27.2
	Reduction rate (%)	77.6%	65.6%	61.4%	55.25%
ARTMD	RMS displacement (mm)	13.6	18.1	16.6	13.6
	Reduction rate (%)	77.6%	70.2%	72.8%	77.6%

As shown in Fig. 11 and Tab. 5, the control effectiveness of unidirectional TRMD continuously decreases with increasing φ_0. In contrast, under the control of ARTMD, the RMS damping ratio of structural displacement response can always be stabilized to more than 70 % after the adaptive direction of ARTMD, and with the increase of initial angle φ_0, the advantage of vibration reduction performance of ARTMD is more enhanced than that of TRMD. This is consistent with the law observed in the numerical simulation, which verifies the actual adaptive adjustment performance of ARTMD.

To further reveal the essence of adaptive vibration reduction of ARTMD, Fig. 12 shows the trend of the angle φ between the track and the displacement direction of the main structure in ARTMD with time. It can be observed that no matter under different initial φ_0, the angle φ will eventually rotate to 0 degrees, which is aligned with the displacement direction of the main structure, thus revealing the essence that ARTMD can achieve adaptive vibration reduction.

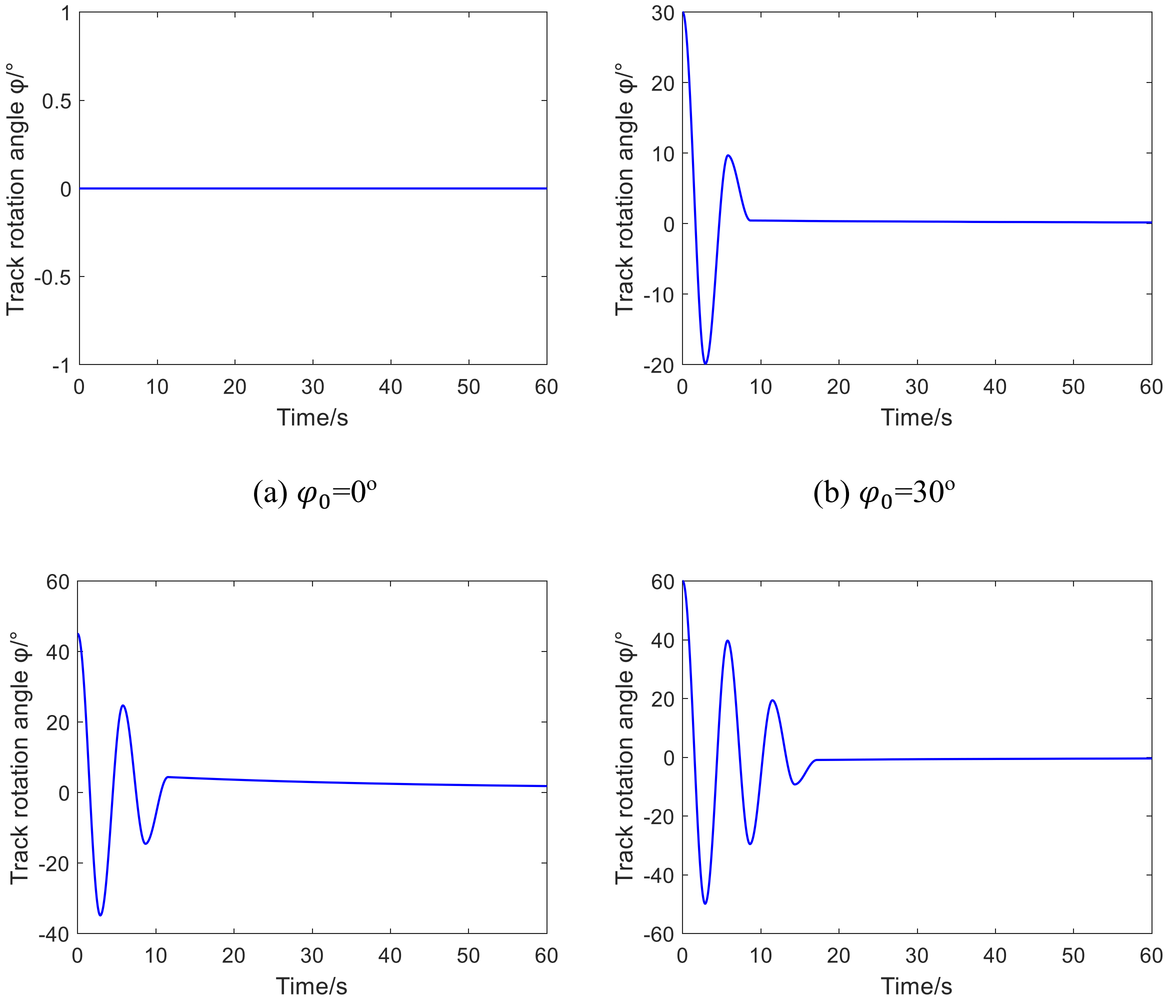

(a) φ_0=0°　　(b) φ_0=30°

(c) φ_0=45°　　(d) φ_0=60°

Fig. 12 Time histories of the track rotational angle φ of different systems with different initial angles φ_0 under harmonic excitation

4.3.3 Random excitation

To better evaluate the vibration reduction performance of ARTMD, in this section, the experimental results of ARTMD under random white noise excitation will be presented. In this experiment, three different types of white noise force excitation are selected. The time history diagram is shown in Fig. 13, which corresponds to standard white noise, low-intensity white noise and high-intensity white noise respectively.

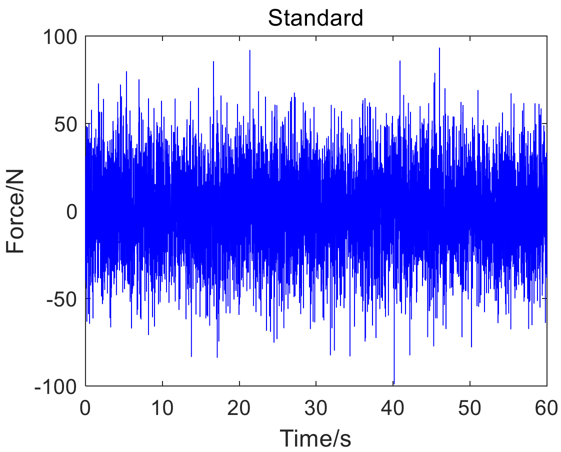

(a)

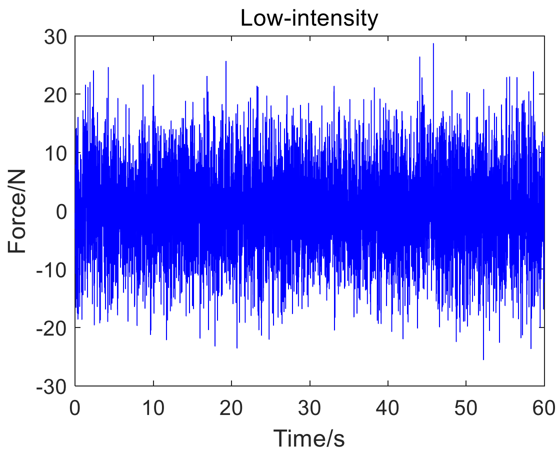

(b)

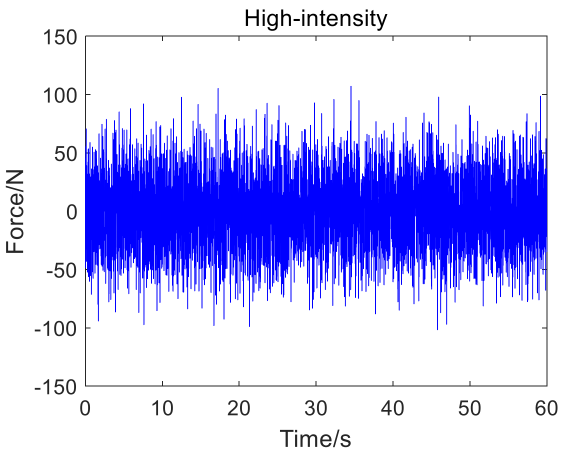

(c)

Fig. 13 Time histories and power spectral density (PSD) of three types of white noise excitation: (a) standard, (b) low-intensity, and (c) high-intensity

Taking the standard white noise excitation as the representative, Fig. 14 describes the displacement time history of the main structure of different vibration reduction systems at four different initial angles φ_0, respectively. Fig. 15 depicts the time history of the track angle φ of ARTMD at different initial angles φ_0. It can be seen from Fig. 14 and Fig. 15 that, thanks to the track adaptive function of ARTMD, when the excitation direction of the main structure is inconsistent with the track direction, the vibration reduction performance of ARTMD is better than that of TRMD, and as the initial angle φ_0 increases, the vibration reduction advantage gradually increases.

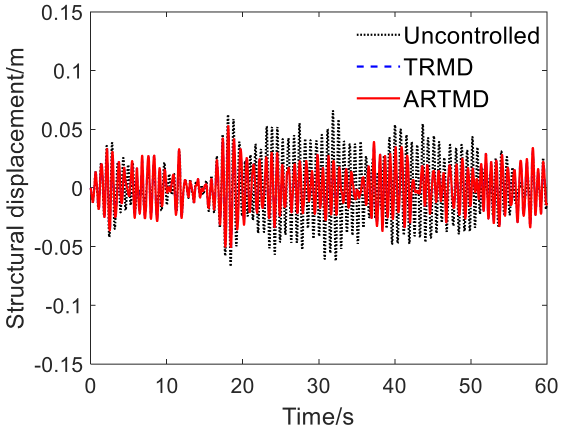

(a) φ_0=0°

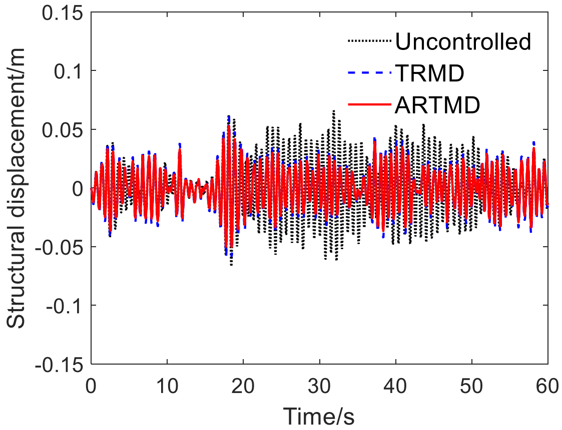

(b) φ_0=30°

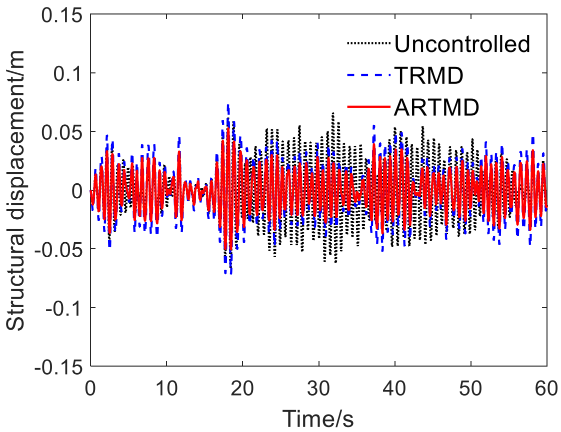

(c) φ_0=45°

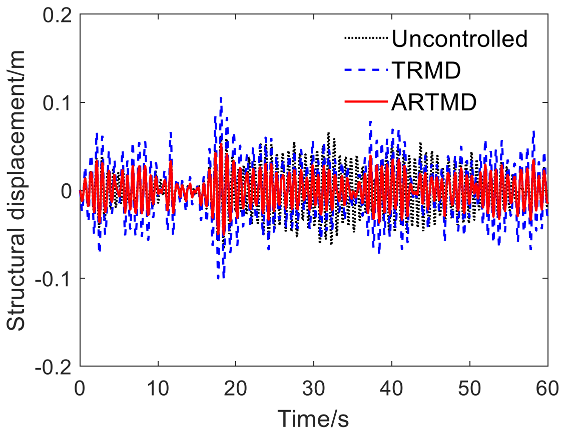

(d) φ_0=60°

Fig. 14 Time histories of the structural displacement with different initial angle φ_0 under standard white noise excitation

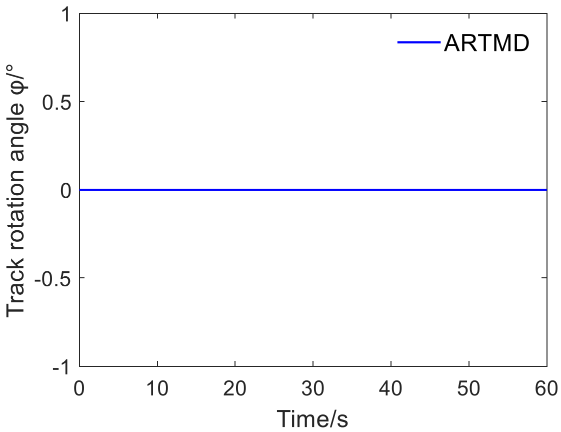

(a) φ_0=0°

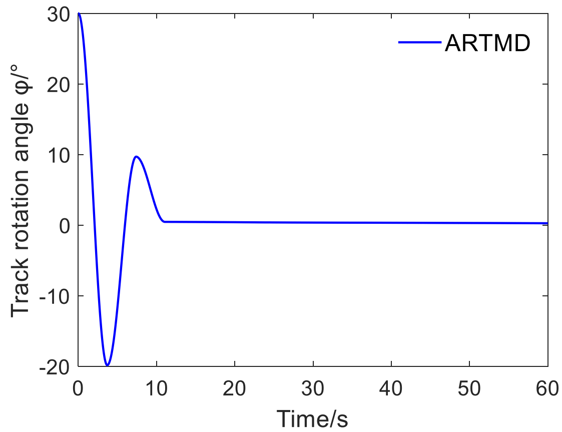

(b) φ_0=30°

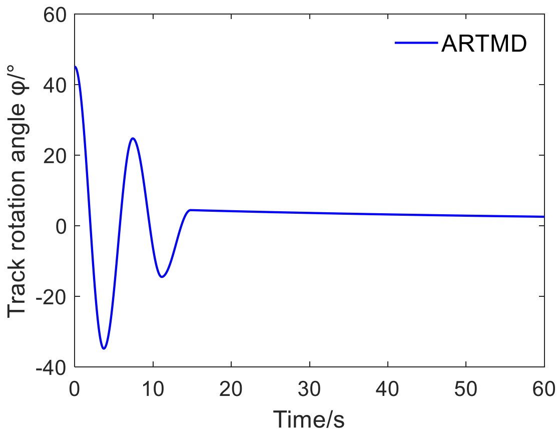

(c) φ_0=45°

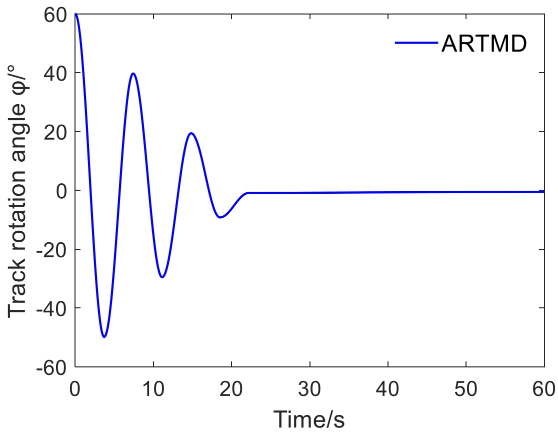

(d) φ_0=60°

Fig. 15 Time histories of the track rotational angle φ of different systems under standard white noise excitation

To evaluate the vibration reduction performance of ARTMD more comprehensively, Table 5 lists the root mean square (RMS) values of the main structure displacement and the response vibration reduction rate of different systems under the three different intensities of white noise excitation. It can be seen that no matter what kind of excitation, when the initial angle φ_0 is 0, the vibration reduction performance of ARTMD and TRMD is consistent, as expected. When the initial angle φ_0 gradually increases, the vibration reduction performance of ARTMD changes little, but the vibration reduction performance of TRMD gradually weakens, which benefits from the track adaptive function of ARTMD.

Tab. 5 The RMS value of structural displacement for different systems under three types of white noise excitation

			φ_0=0°	φ_0=30°	φ_0=45°	φ_0=60°
Standard white noise excitation	UC	RMS displacement (mm)	24.6	24.6	24.6	24.6
	TRMD	RMS displacement (mm)	16.5	19.1	23.4	33.0
		Reduction rate (%)	32.9%	22.5%	5.1%	-34.2%
	ARTMD	RMS displacement (mm)	16.5	16.5	16.5	16.5
		Reduction rate (%)	32.9%	32.9%	32.9%	32.9%
Low-intensity white noise excitation	UC	RMS displacement (mm)	13.5	13.5	13.5	13.5
	TRMD	RMS displacement (mm)	6.6	7.7	9.4	13.3
		Reduction rate (%)	50.8%	43.2%	30.4%	14.5%
	ARTMD	RMS displacement (mm)	6.6	6.6	6.6	6.6
		Reduction rate (%)	50.8%	50.8%	50.8%	50.8%
High-intensity white noise excitation	UC	RMS displacement (mm)	42.6	42.6	42.6	42.6
	TRMD	RMS displacement (mm)	24.2	28.0	34.3	48.4
		Reduction rate (%)	43.2%	34.4%	19.7%	-13.6%
	ARTMD	RMS displacement (mm)	24.2	24.2	24.2	24.2
		Reduction rate (%)	43.2%	43.2%	43.2%	43.2%

5 Conclusion

To address the vibration control requirements for structures in random directions, an adaptive rolling tuned mass damper (ARTMD) is proposed in this paper. To analyze the performance of the ARTMD, a dynamic model of a SDOF structure coupled with a ARTMD is established. The parametric optimization of the ARTMD is conducted based on the H_∞ optimization criterion, whose object is to minimize the maximum structural displacement. Then, numerical simulations and experiments are conducted to evaluate the performance of the ARTMD. The specific conclusions are the following:

(1) The main parameter of ARTMD is the tuning frequency ratio. After optimizing the design of ARTMD, when the track direction is inconsistent with the vibration direction, the vibration reduction performance of ARTMD is better than that of TRMD with the same mass ratio, mainly due to the track adaptive function of ARTMD. In addition, among the other structural design parameters, the friction coefficient of the track has a greater influence, while other parameters have less influence.

(2) The experimental results show that whether under free vibration, harmonic excitation or random excitation, the vibration reduction performance of ARTMD is better than that of TRMD when the track direction and vibration direction are inconsistent, which further confirms the adaptive vibration reduction function of ARTMD. Moreover, with the increase of the angle, the vibration reduction advantage of ARTMD is greater.

Acknowledgement

The authors wish to thank the partial financial support from the National Natural Foundation of China (grant # 52308001, W2411050), Hunan Provincial Key Laboratory Project of China (grant # E22439) , Hunan University of Science and Technology Research Project of China (grant # E523D4) and Hunan College Students' Innovative Development Project of China (grant # S202510534187)

References

[1] Housner G W, Bergman L A, Caughey T K, et al. Structural Control: Past, Present, and Future. Journal of Engineering Mechanics, 1997, 123(9): 897-971.

[2] Chen S, Wang W, Liu G, et al. Mechanical behavior and seismic control performance of a metallic torsional damper for flexible structures. Engineering Structures, 2024, 318: 118674.

[3] Song Y, Li Z, Ning J, et al. Dynamic characteristics and vibration reduction performance of a novel Bi-TRMD. Journal of Southeast University (English Edition), 2025, 41(2): 148-155.

[4] Dyk Š, Bulín R, Rendl J. Nonlinear dynamics of ball vibration absorber considering stability, stationarity and rolling-condition boundaries. Journal of Sound and Vibration, 2025: 119265.

[5] Pirner M. Dissipation of kinetic energy of large-span bridge. Acta technica CSAV, 1994, 39: 645-647.

[6] Pirner M, Fischer O. The development of a ball vibration absorber for the use on towers. Journal of the International Association for Shell and Spatial Structures, 2000, 41(2): 91-99.

[7] Pirner M. Actual behaviour of a ball vibration absorber. Journal of Wind Engineering and Industrial Aerodynamics, 2002, 90(8): 987-1005.

[8] Fischer O. Wind-excited vibrations-solution by passive dynamic vibration absorbers of different types. Journal of Wind Engineering and Industrial Aerodynamics, 2007, 95(9-11): 1028-1039.

[9] Jie L, Zili Z, Jianbing C. Experimental study on vibration control of offshore wind turbines using a ball vibration absorber. Energy and Power Engineering, 2012, 4: 153-157.

[10] Zhang Z L, Chen J B, Li J. Theoretical study and experimental verification of vibration control of offshore wind turbines by a ball vibration absorber. Structure and Infrastructure Engineering, 2014, 10(8): 1087-1100.

[11] Zhang Z, Li J, Nielsen S R K, et al. Mitigation of edgewise vibrations in wind turbine blades by means of roller dampers. Journal of Sound and Vibration, 2014, 333(21): 5283-5298.

[12] Chen J, Georgakis C T. Tuned rolling-ball dampers for vibration control in wind turbines. Journal of Sound and Vibration, 2013, 332(21): 5271-5282.

[13] Chen J, Wang Y, Zhao Y, et al. Experimental research on design parameters of basin tuned and particle damper for wind turbine tower on shaker. Structural Control and Health Monitoring, 2019, 26(11): e2440.

[14] Li S, Fu L, Kong F. Seismic response reduction of structures equipped with a voided biaxial slab-based tuned rolling mass damper. Shock and Vibration, 2015, 2015(1): 760394.

[15] Sun L, Li S, Zhang F. Effect of self-resetting ball absorber on the mechanical properties of the fabricated structure and its influencing factors: Theory and Experimentation. Journal of Vibration Engineering & Technologies, 2022, 10(3): 897-917.

[16] Li S, Sun L, Kong F. Vibration control performance analysis and shake-table test of a pounding tuned rotary mass damper under the earthquake. Shock and Vibration, 2019, 2019(1): 4038657.

[17] Mao L, Li S, Yang C, et al. Friction influence on the pounding tuned rotary mass damper: Modeling, numerical simulation and experiment validation. Journal of Sound and Vibration, 2022, 536: 117146.

[18] Bransch M. Unbalanced oil filled sphere as rolling pendulum on a flat surface to damp horizontal

structural vibrations. Journal of Sound and Vibration, 2016, 368: 22-35.

[19] Obata M, Shimazaki Y. Optimum Parametric Studies on Tuned Rotary-Mass Damper. Journal of Vibration and Control, 2008, 14(6): 867-884.

[20] Yang S, Zhang X, Dong Y, et al. Research on restraint of human arm tremor by ball-type dynamic vibration absorber. Journal of Measurement Science and Instrumentation (English Edition), 2023, 14(4): 425-430.

[21] Xiang Y, Tan P, He H, et al. A novel bi-directional rail variable friction pendulum-tuned mass damper (BRVFP-TMD). Mechanical Systems and Signal Processing, 2023, 197: 110396.

[22] Xiang Y, Tan P, Wu J, et al. Bi-directional wind-induced vibration control of high-rise buildings using bi-directional rail variable friction pendulum-tuned mass damper. Engineering Structures, 2024, 303: 117557.

[23] Jahangiri V, Sun C. Three-dimensional vibration control of offshore floating wind turbines using multiple tuned mass dampers. Ocean Engineering, 2020, 206: 107196.

[24] Jahangiri V, Sun C, Kong F. Study on a 3D pounding pendulum TMD for mitigating bi-directional vibration of offshore wind turbines. Engineering Structures, 2021, 241: 112383.

[25] Jahangiri V, Sun C, Babaei H. Application of a new two dimensional nonlinear tuned mass damper in bi-directional vibration mitigation of wind turbine blades. Engineering Structures, 2024, 302: 117371.

[26] Ding H, Wang J T, Lu L Q, et al. Parameter optimization of toroidal tuned liquid column dampers for suppressing multi-directional harmonic vibration of structures. Engineering Optimization, 2022, 54(1): 1-19.

[27] Zhang J, Ding H, Wang J T. A semi-active toroidal TLCD for multidirectional vibration reduction of structures. Smart Materials and Structures, 2022, 31(12): 125006.

[28] Wang L, Zhou Y, Nagarajaiah S, et al. Bi-directional semi-active tuned mass damper for torsional asymmetric structural seismic response control. Engineering Structures, 2023, 294: 116744.

[29] Wang L, Zhou Y, Shi W. Random crowd-induced vibration in footbridge and adaptive control using semi-active TMD including crowd-structure interaction. Engineering Structures, 2024, 306: 117839.

[30] Hu R, Yang M, Meng D, et al. Robustness investigation of Horizontal Bidirectional Hybrid Damping

System applied to long-span bridges under near-fault pulse-like earthquakes. Soil Dynamics and Earthquake Engineering, 2024, 184: 108803.

[31] Hu R, Yang M, Meng D, et al. Seismic fragility analysis of a long-span cable-stayed bridge equipped with a horizontal bidirectional hybrid damping system. Structure and Infrastructure Engineering, 2025: 1-14.

[32] Lei Z, Liu G, Cong Y, et al. Research on fatigue damage mitigation of offshore wind turbines by a bi-directional PSTMD under stochastic wind-wave actions. Engineering Structures, 2024, 301: 117275.

[33] Náprstek J, Fischer C. Non-holonomic dynamics of a ball moving inside a spherical cavity. Procedia Engineering, 2017, 199: 613-618.

[34] Náprstek J, Fischer C. Stable and unstable solutions in auto-parametric resonance zone of a non-holonomic system. Nonlinear Dynamics, 2020, 99(1): 299-312.

[35] Náprstek J, Fischer C. Limit trajectories in a non-holonomic system of a ball moving inside a spherical cavity. Journal of Vibration Engineering & Technologies, 2020, 8(2): 269-284.

[36] Náprstek J, Fischer C. Trajectories of a ball moving inside a spherical cavity using first integrals of the governing nonlinear system. Nonlinear Dynamics, 2021, 106(3): 1591-1625.

[37] He H, Tan P, Hao L, et al. Optimal design of tuned viscous mass dampers based on effective damping ratio enhancement effect. Journal of Sound and Vibration, 2022, 534: 117018.

[38] Chen H, Tan P. Optimal design of TVMD with linear and nonlinear viscous damping subjected to white-noise excitation. Structural Control and Health Monitoring, 2021, 28(4): e2694.

[39] Luo Y, Sun H, Zhang Z, et al. Analytical optimization of the rotational inertia double tuned mass damper for structures under random excitation. Structures, 2024, 69: 107462.

[40] Luo Y, Gao J, Peng J, et al. Strongly modulated response and bifurcation characteristics of a lever-type nonlinear energy sink. Nonlinear Dynamics, 2025: 1-28.